Journal of the American Ceramic Society

On Compressive Brittle Fragmentation

Journal:	*Journal of the American Ceramic Society*
Manuscript ID	Draft
Manuscript Type:	Article
Date Submitted by the Author:	n/a
Complete List of Authors:	Hogan, James; University of Alberta, Mechanical Engineering Farbaniec, Lukasz; John Hopkins Engineering, Department of Mechanical Engineering Daphalapurkar, Nitin; Johns Hopking University, Mechanical Engineering Ramesh, K.; John Hopkins Engineering, Department of Mechanical Engineering
Keywords:	silicon carbide, fracture mechanics/toughness, brittle materials, particle size distribution, strength
Note: The following files were submitted by the author for peer review, but cannot be converted to PDF. You must view these files (e.g. movies) online.	
Compre_Frag_wNitin_v3.tex	

On Compressive Brittle Fragmentation

James David Hogan[a,b], Lukasz Farbaniec[b], Nitin Daphalapurkar[c], K.T. Ramesh[b,c]

[a]*Department of Mechanical Engineering, The University of Alberta, Edmonton, AB T6G 2R3, Canada*
[b]*Hopkins Extreme Materials Institute, The Johns Hopkins University, Baltimore, MD 21218, USA*
[c]*Department of Mechanical Engineering, The Johns Hopkins University, Baltimore, MD 21218, USA*

Abstract

Dynamic brittle fragmentation is typically described using analytical and computational approaches for tensile stress-states. However, most fragmentation applications (e.g., impact, blast) involve very large initial compressive stresses and deformations. In this study, the compressive fragmentation of brittle materials is investigated experimentally across a range of materials: silicon carbide, boron carbide, spinel, basalt and a stony meteorite. Analysis of our experimental results suggests there exists two different regimes in the fragment size distributions, based on two brittle fragmentation mechanisms. The first is a mechanism that produces larger fragments and is associated with the structural failure of the sample being tested. This mechanism is influenced by the loading conditions (rate, stress state) and sample geometry. The second fragmentation mechanism produces comparatively smaller fragments and arises from the coalescence of fractures initiating and coalescence between defects in regions of large stresses and contact forces (e.g., between two fractured surfaces from the larger fragments). A framework is developed for comparing experimental compressive fragmentation results with tensile fragmentation theories. The compressive experimental results are shown to be adequately described by the theories using the new framework.

Email address: jdhogan@ualberta.ca (James David Hogan)

Preprint submitted to Journal of the American Ceramic Society *October 25, 2015*

Keywords: compressive fragmentation; brittle failure; experimental mechanics; advanced ceramics;

1. Introduction

Understanding the fragmentation of brittle materials is important in defense and shielding applications [1], planetary and space science [2], and blasting and mining industries [3]. It is of particular interest to develop predictive capabilities for the resulting fragment size distributions, whether for specific applications like impact [4] and grinding [5], or more generally as a function of the rate of loading and the stress state.

Many of the past investigations on fragmentation have been concerned with tensile stress-states. Among them, Mott [6, 7] pioneered early studies on fragmentation. He considered the origin of fracture sites within an idealized geometry and the propagation of tensile release waves away from these fracture sites. Grady [8] refined Mott's approach through consideration of the instantaneous occurrence of fracture and the statistical properties of failure. Grady's energy-based tensile fragmentation theory compared the kinetic energy of expansion to the energy required to create new fragment surfaces. Later, Glenn and Chudnovsky [9] extended the work of Grady [8] to include the contribution of elastic strain energy at low strain-rates. More recently, Zhou et al. [10, 11] and Levy and Molinari [12] developed predictions of the rate-dependent average fragment size using results from the numerical simulation of expanding brittle rings, incorporating localized cohesive zones for energy dissipation. These numerical models are able to capture the evolution of the residual damage and elastic wave interactions, which the simple energy-based analytical models are not able to accommodate.

Although typical fragmentation models consider purely tensile stress-states, the applications described earlier generally involve very large initial compressive stresses and

deformations. These initial compressive domains have at least three major effects on the fragmentation problem. First, they pre-condition the loaded material by creating, activating and growing internal defects, so that the fragmenting material is quite different from the pristine unloaded material. Second, some fracture can occur even under compression, such as through the wing-crack mechanism [13, 14]. Third, the compressed material stores substantial amounts of strain energy that can be released in the subsequent fragmentation process. We seek to understand some of these effects in this work, recognizing that the degree to which these effects become dominant are strongly dependent on the material in question.

There are many types of brittle materials, each with varying composition, strength, density, hardness, grain size, and secondary phases. The individual phases also have varying mechanical properties. The dynamic failure of many brittle materials have been studied, including: advanced ceramics (e.g., boron carbide [15], silicon carbide [16], and spinel [17]), glasses [18], brittle plastics (e.g., homalite [19]), cement-based composites (e.g., [20]), and rocks (e.g., basalt [21] and granite [22]) and minerals (e.g., quartz [5]). The failure of brittle materials is generally a result of the initiation, growth and coalescence of cracks originating from microstructural defects. "Defects" include secondary phases, grain boundaries between similar and dissimilar materials, and pre-existing micro-cracks and surface flaws. For example, advanced ceramic materials such as silicon carbide are commonly sintered with additives to enhance ease of processing. These additives can agglomerate to form secondary phases. In silicon carbide, carbonaceous and second ceramic processing-induced defects tend to serve as sites for fracture initiation [23, 24]. Understanding which defects contribute to failure (and then fragmentation) is of fundamental importance to material modelling and design.

This study augments the reviews by Ryan [25], Zhang and Zhao [26] and Ramesh et

al. [27], which highlight the need for more detailed consideration of compressive brittle fragmentation. In this paper, the dynamic compressive fragmentation of brittle materials is investigated. A hot-pressed silicon carbide is considered as a model brittle material, but results are also discussed from other published works on a hot-pressed boron carbide [15], spinel [17], basalt [21], and a stony meteorite (GRO 852090) [28]. The key microstructural features in this silicon carbide are identified, and image processing methods are presented for quantifying these features. Links are then made between the microstructural features, compressive failure mechanisms, and fragmentation size and shape distributions. While the analysis is similar to that previously published for boron carbide [15], the results presented here for silicon carbide are more in-depth, as well as are essential for the flow of the paper (i.e., the fragmentation results link with the Scanning Electron Microscope images and high-speed images during experimentation). A framework for comparing compressive brittle fragmentation results with tensile theories is then presented. A prediction for the rate-dependent average fragment size in compression is derived by extending the Grady [8], and Glenn and Chudnovsky [9] analytical forms. A further discussion of fragmentation may be found in Grady [8], and an additional resource on both ductile and brittle fragmentation is provided by the book by Grady [29].

2. Experimental Setup and Materials

Fragmentation is generated in uniaxial compression experiments in brittle materials under both quasi-static and dynamic conditions. The quasi-static experiments are performed with an MTS servo-hydraulic test machine with a controlled displacement rate at strain rates of 10^{-4} to 10^{-3} s^{-1}. The dynamic experiments are performed using a Kolsky bar apparatus for strain rates between 100 and 1,000 s^{-1}. Both testing platforms are de-

scribed in Kimberley et al. [30] and experimental design is discussed therein. Cuboidal specimens (5.3 mm in length by 4 mm by 3.5 mm) are used and failure is imaged on one of the faces during loading with a Specialised Imaging SIMD Camera operating at 1.1 Mfps with a 400 ns exposure time. A Zeiss optical microscope with an AxioCam MRC camera is used to quantify the material microstructure and to characterize the fragments post-mortem. A TESCAN MIRA Scanning Electron Microscope (SEM) with Energy Dispersive Spectroscopy (EDS) capabilities is used to identify the composition of constituent phases in the microstructure, as well examine fracture surfaces post-experiment.

The materials examined in this study are:

1. A hot-pressed silicon carbide (PAD SiC-N) from Coorstek (Vista, California). A similar material was used in the study by Wang and Ramesh [16], and Bakas et al. [24].
2. A hot-pressed boron carbide (PAD B4C) from Coorstek (Vista, California). This material was used in the study by Hogan et al. [15, 31] and Farbaniec et al [14].
3. A transparent spinel ($MgAl_2O_4$) with average grain size of 0.4 μm. This material was one of two spinels examined by Kimberley and Ramesh [17], and was produced by Krell et al. [32].
4. A basalt rock material purchased from Coverall Stone, WA consisting of olivine, pyroxene, and feldspar. This material was studied by Stickle et al. [33], and Hogan et al. [21].
5. A stony meteorite material (GRO 85209), which is an L6 chondrite consisting primarily of low-Ca pyroxene and iron-nickel, with some olivine and chondrules [34]. This material was studied in Hogan et al. [28, 35].

Examples taken from the silicon carbide are used throughout the paper to help establish the observed failure and fragmentation mechanisms in these brittle materials. Later, experimentally measured fragment sizes for all materials are compared against fragmentation model predictions.

A summary of density (ρ: kg/m^3), Young's modulus (E: GPa), and fracture toughness (K_{1c}: MPa $\sqrt{m}$) for all materials in this study are shown in Table 1. Values for the PAD SiC-N and PAD B4C are taken from the Coorstek data sheet. Values for spinel are taken from Kimberley and Ramesh [17]. For basalt, density and Young's modulus are taken from Stickle et al. [33]. A fracture toughness value for basalt of 1.6 MPa $\sqrt{m}$ is taken from Balme et al. [36], noting that this value is used by Tonge et al. [37] in simulations of asteroid impacts. Lastly, as no fracture toughness measurements were available on the meteorite samples, they are assumed to have a lower fracture toughness than that of basalt (here 1.2 MPa $\sqrt{m}$). All other values for the meteorite are measured in Hogan et al. [35].

3. Experimental Results

In this section, links are made between the microstructural features and the compressive failure and fragmentation of silicon carbide. Initially, the key microstructure defects in this silicon carbide are identified and methods to quantify the size and spacing of these defects are presented. The dynamic compressive failure mechanisms are examined using high-speed photography during Kolsky bar testing, and then optical and scanning electron microscopy is used to probe what types of defects contributed to that failure. Fragment size and shape distributions are then explored, and correlations are made between fragmentation mechanisms, the microstructure, and the structural failure of the sample. Failure modes, key defects, and fragmentation results for boron carbide [15],

basalt [21], and GRO 85209 [28] are discussed in their associated references.

3.1. Silicon Carbide Microstructure

The microstructural features in the PAD SiC-N are introduced in the optical microscope image in Figure 1. The grain sizes of the silicon carbide are between 5 to 15 μm (confirmed with SEM). The optical micrograph image shows two types of microstructural features: 1. bright features, which have been identified as Al/Fe-rich phase in composition using EDS. These features are also observed in Bakas et al. [24], and 2. dark features, which are primarily holes that contain traces of the Al/Fe-rich phase. It is speculated that grains (or phases) pop-out during sample preparation. These bright and dark features are much less than 10 μm in size. Interestingly, we have not identified any carbonaceous inclusions in our hot-pressed silicon carbide microstructure. Carbonaceous inclusions have been found in the silicon carbides of Wang and Ramesh [16], and Bakas et al. [24], indicating that our material is different.

Also shown in Figure 1, are methods for determining the size, orientation, and defect density (#/m^2) and spacing of the features. Later, defect spacing is linked with the fragment sizes, and this allows us to more definitively determine which microstructure feature is important in fragmentation. To determine the defect statistics, image processing techniques in Matlab [38] are used. First, images of the microstructure are taken using an optical microscope. A thresholding algorithm is applied to the images that converts the images to monochrome (see Figure 1). Also highlighted in the green box in the figure is a further magnified monochrome image of a bright Al/Fe phase. This shows the resolution at which the statistics are computed. Once the optical microscope images are converted to monochrome, the image processing toolbox is used to determine the size ($2s$: taken as the length of the largest spanning dimension of a fitted

ellipse), orientation (direction of major axis of the fitted ellipse), and centroids of each of these microstructure features. The distance between the centroids of adjacent features is defined as the defect spacing (ℓ_n). An additional discussion of the image processing methods can be found in Hogan et al. [15].

3.2. Dynamic Uniaxial Compressive Failure

The macroscopic failure mechanisms in silicon carbide during dynamic uniaxial compression are shown in Figure 2, which shows a stress-time history curve (on the left) with time-resolved high-speed photography images (on the right) for a typical uniaxial dynamic compression experiment. The stress rate, $\dot{\sigma}$, is shown using a dashed line on the left and is 255 MPa/μs for this experiment. This is determined as the slope of the stress-time plot between 10 and 90 % of the peak stress, which is 5.3 GPa for this experiment. Assuming linear elasticity, the corresponding strain rate, $\dot{\epsilon}$, is estimated by dividing the stress rate by the Young's modulus.

At times t_1 and t_2 (prior to peak stress), there are no cracks visible on the surface. Failure is first observed on the imaged surface at t_3, and occurs on the top right corner of the sample. As a result of failure and fracture, the material stiffness degrades, and the stress in the sample begins to decrease. At time t_4, axial cracks are observed to span across the sample, and the stress in the sample continues to collapse. At time t_5, many more axial cracks are observed to span the sample and these form columnar structures. In addition to more axial cracks, fractures perpendicular, or transverse, to the loading direction are now observed. Transverse cracks are believed to occur as a result of the buckling of the columns created from axial cracks, as described by Ashby and Hallam [39]. On average, the velocity of the axial cracks is 1,700±400 m/s, as measured by tracking the crack tips of the first few cracks on the imaged surface over multiple

camera frames. At later times (t_6), additional axial and transverse cracks rapidly develop across the sample, these cracks coalesce, and the stress in the material collapses. The coalescence of axial and transverse cracks at time t_6 results in the generation of larger fragments that are between 100 and 2,000 μm in size.

Also first observed at t_5 are brighter features (clouds) at the left side and in the centre of the sample. These are highlighted in t_6, where they now become more visible between the two times. These features are believed to arise from very fine fragments, much smaller than the fragments formed from the coalescence of axial and transverse fractures. This fines have not been previously observed high-speed images in studies involving boron carbide (e.g., [28]), possibly suggesting differences in their failure characteristics. We will show that this dust is a consequence of intergranular fracture in silicon carbide, compared to transgranular fracture in the hot-pressed boron carbide [15]. This fragmentation mechanism is explored later.

3.3. Microstructural Consequences for Failure

Next we examine fracture surfaces in Figure 3a and b. The scanning electron microscope image in Figure 3a indicates that fracture is primarily intergranular in nature and that there is debris on the fracture surface. As mentioned before, we believe that the fines observed in the high-speed video images and on the surface is a consequence of intergranular fracture and subsequent abrasion between surfaces. Shown in Figure 3b is an SEM image of the fracture surface using the back-scattered electron detector, allowing one to visualize compositional differences on the fracture surface. Multiple Al/Fe phases are observed on the fracture surface (composition confirmed with EDS), suggesting that these may serve as fracture initiation sites in this hot-pressed silicon carbide material. We refer to the Al/Fe phases as ”defects” hereafter. These observations

are different than those by Wang and Ramesh [16], and Bakas et al. [24] who noted that the carbonaceous defects were primary sites for fracture initiation. However, we do not observe any carbonaceous defects in this material.

3.4. SiC-N Fragmentation

This subsection establishes relationships between the fragment sizes, the defect spacing, and the fragmentation mechanisms. As with the microstructure characterization, images of a collection of fragments are taken and converted to monochrome using thresholding. Image processing in Matlab [38] is used to determine their major axis size (ℓ), projected area (A) and perimeter (P) in the image. Following terminology outlined by Hogan et al. [15] in their study on boron carbide fragmentation, one can define the cumulative distribution function:

$$G(x) = \int_0^x g(\bar{x}) d\bar{x} \tag{1}$$

where the probability distribution of fragment sizes, $\bar{x}$, is $g(\bar{x})$. The fragment size data set is a discrete set of N fragments with sizes ℓ_i (i=1...N). Ordering this data for increasing fragment size, and assigning a probability of $1/N$ to each fragment, the empirical cumulative distribution function (eCDF) is as the sum of these probabilities:

$$G_e(\ell) = \frac{1}{N} \sum_{i=1}^{N} I(\ell_i \leq \ell) \tag{2}$$

where the indicator function I has a value of 1 if $\ell_i \leq \ell$ and 0 otherwise. Figure 4 shows the empirical cumulative distribution of the fragment major axis size for fragments derived from uniaxial compression at a quasi-static strain rate of 10^{-4} s^{-1} (dashed green curve) and a dynamic strain rate of 490 s^{-1} (dotted curve). For both strain rates, the

resolution of the camera sets the lower limit of fragment sizes at approximately 10 μm, which approximately corresponds 15 pixels in total area.

As expected, the curves shift to the left as the strain rate is increased. This is likely a consequence of two related factors: (1) there is additional strain energy absorbed by the material when it is loaded dynamically, thus requiring more fractures to dissipate that energy; and (2) more defects are activated at higher rates, thus facilitating additional fracturing during failure. For both quasi-static and dynamic distributions, an inflection in the eCDF is noted at approximately 60 μm (as shown by the red line). This indicates that two different fragmentation mechanisms may be present. We divide the distributions in Figure 4 by fragment size at a size of 60 μm, with the domain ℓ_i<60 μm called fragmentation Regime I, and that with ℓ_i>60 μm called Regime II. Regime I comprises 6 % of the total population for quasi-static case and 18 % for the dynamic case.

A possible explanation for the existence of these two regimes is provided by the eCDF of the Al/Fe defect spacing in the microstructure, presented as the blue curve in Figure 4. Very nearly all of the spacings are less than 60 μm apart, suggesting that the Regime I upper boundary may be related to the spacings between adjacent Al/Fe defects. In this fragmentation mechanism, cracks initiated from the defects are believed to coalesce with fractures initiated at other defects. Fracture is believed to be promoted through abrasion of the fracture surfaces formed through intergranular fracture. This is consistent with previously observed optical microscopy and SEM measurements (Figure 3). Because these microstructural spacings correlate with Regime I, we call this regime the microstructure-controlled fragmentation regime [15]

Additional insight into the two fragmentation regimes is obtained by plotting the fragment circularity against size in Figure 5 for a dynamic experiment. The circularity,

Φ, is defined as:

$$\Phi = \frac{r_1}{r_2} = \frac{\sqrt{A/\pi}}{P/2\pi} = \frac{2\sqrt{\pi A}}{P} \tag{3}$$

where r_1 is the equivalent radius of a fragment determined from its area (A), and r_2 is the equivalent radius of a fragment determined from its perimeter (P). For the case of a circle, the circularity is equal to 1. We note that fragments with $\Phi > 1$ typically arise from pixelation errors in the optical imaging process for fragments < 20 μm in size (labelled as "low accuracy region" in the figure). The two fragmentation regimes are clearly defined in Figure 5, where distinct clustering is apparent. *Regime I* has a circularity greater than 0.4 and fragment sizes <60 μm. We refer to the Regime I fragmentation mechanism as microstructure-dependent because of the correlation with the microstructure length scales in the defect spacing. This mechanism becomes more important as the strain-rate is increased, as shown in Figure 4. *Regime II* has a circularity between 0.5 and 0.9 and fragment sizes >60 μm. We define $\ell_{II\ min}$ as the lower limit of Regime II. We believe Regime II fragments are comprised of larger fragments formed from the structural collapse mechanism previously observed in high-speed camera images in Figure 2, and described by Ashby and Hallam [39]. This fragmentation mechanism is structural-dependent, in that the fragment sizes are determined by which macroscopic failure modes are available, which in turn is related to structural geometry and boundary conditions. As this regime of fragments trends to larger sizes, their circularity decreases as a result of becoming more blocky. This is reasonable, since the larger fragments are believed to be formed from the coalescence of axial and transverse cracking (hence they are nominally more rectangular/blocky than smaller ones). At the same time, the greater scatter in the circularity of Regime I is a result of the greater irregularity in shapes for the smaller fragments. Lastly, the non-smooth transition between the two regimes is

believed to be a consequence of the different formation mechanisms.

4. Brittle Fragmentation Theory

This section presents current models describing brittle fragmentation, and a framework that allows the experimental compressive fragmentation results to be compared with the models. We conclude this section with analysis of the structural-dependent fragment size distributions.

4.1. Current Models

Four of the major models predicting the rate-dependent average fragment size include: the analytical predictions by Grady [8], and Glenn and Chudnovsky [9], and predictions derived from the simulations of expanding brittle rings by Zhou et al. [10, 11], and Levy and Molinari [12]. Grady has presented several refinements of his model, and we choose the form from reference [8] because it compares easily with the Glenn and Chudnovsky [9] predictions for higher rates. Prior to introducing the models, characteristic terms compiled by Zhou et al. [11] in their numerical study of brittle fragmentation using cohesive elements are presented since these can be used to normalize the fragment sizes and strain rates for comparative purposes among the many types of brittle materials that we investigate in this study.

First, a characteristic time t_0 was proposed by Camacho and Ortiz [40] on the basis of a cohesive zone and wave propagation:

$$t_0 = \frac{E\Gamma}{\sigma_t^2 c} \tag{4}$$

where E is the Young's modulus (Pa), Γ is the fracture energy (J/m^2), c is the longitudinal speed of sound in the material (m/s), σ_t is the *quasi-static tensile* strength of the

material (Pa), and Γ is the failure energy (J/m^2). In this case, Γ it is taken as the fracture energy for plane stress conditions given as:

$$\Gamma = \frac{K_{Ic}^2}{2E} \tag{5}$$

where K_{Ic} is the fracture toughness (MPa $\sqrt{m}$). The characteristic size of the cohesive zone L_0 is then:

$$L_0 = ct_0 \tag{6}$$

Lastly, the characteristic strain rate first defined by Drugan[41] is given as:

$$\dot{\epsilon}_0 = \frac{\sigma_t}{Et_0} = \frac{2\sigma_t^3 c}{EK_{Ic}^2} \tag{7}$$

Values for K_{Ic}, ρ, E for each material were previously shown in Figure 1. The values for the *quasi-static strength* are taken as σ_t=$\sigma_{c\ qs}/\alpha$, where $\sigma_{c\ qs}$ is the quasi-static compressive strength. We note that α is dependent on, among other things, the distribution of defects in the material (activated defects may be different in compression and tension, and for different materials). Lacking specific data, we take α=10, which is motivated by the compilation of tensile and compressive strength measurements found in Charles [42]. This simplification is used due to the lack of quasi-static tensile strength measurements performed for these materials (these are hard to perform regardless).

The current tensile models predicting the rate-dependent fragment size can be compared in terms of normalized sizes and strain rates, with the fragment size normalized by L_0 and the strain rate normalized by $\dot{\epsilon}_0$. The predicted normalized average fragment

size proposed by Grady [8] is:

$$\bar{L}_{Grady} = \left(\frac{24}{\bar{\dot{\epsilon}}^2}\right)^{1/3} \tag{8}$$

where the bar denotes that the term is normalized. The Glenn and Chudnovsky [9] normalized average fragment size is:

$$\bar{L}_{GC} = \frac{4}{\bar{\dot{\epsilon}}} sinh\left(\frac{1}{3} sinh^{-1}\left(\frac{3}{2}\,\bar{\dot{\epsilon}}\right)\right) \tag{9}$$

The Zhou et al. [10, 11] normalized average fragment size is:

$$\bar{L}_{ZMR} = \frac{4.5}{1 + 4.5\bar{\dot{\epsilon}}^{2/3}} \tag{10}$$

and the Levy and Molinari [12] normalized average fragment size is:

$$\bar{L}_{LM} = \frac{3}{1 + 4.5\bar{\dot{\epsilon}}^{2/3}} \tag{11}$$

The coefficients in the models by Zhou et al. [10, 11], and Levy and Molinari [12] were obtained by fits to their expanding ring simulation data, while the Grady [8], and Glenn and Chudnovsky [9] are based on energy balances.

We develop a modified version of the model by Grady [8], which we then extend to the Glenn and Chudnovsky [9] model. We assume that fractures grow at a speed of v_c (m/s) rather than c (as suggested in Grady [8]) during failure for a time of t so that the length scale is:

$$\hat{L}_{Grady} = 2v_c t \tag{12}$$

The $\hat{L}_{Grady}$ represents the modified form of the original model. To determine t, the

approach of Grady [8] is used wherein the volumetric strain energy density (U_e) and the fracture energy density (U_s) [8] are equated, where U_e in compression is defined as:

$$U_e = \frac{1}{2}E\epsilon^2 = \frac{1}{2}E\dot{\epsilon}^2 t^2 \tag{13}$$

The fracture energy density is:

$$U_s = \frac{C\Gamma}{v_c t} \tag{14}$$

where C is a scaling coefficient that is based on the dimensionality of the problem [8] (e.g., C=3 for volumetric problem and C=2 for an expanding ring).

We also define the ratio of the time that it takes to absorb the strain energy ("loading time": t^ℓ) to the time that it takes to dissipate that energy through fracture ("failure time": t^f) as M=t^ℓ/t^f. We note that t^ℓ is dominated by the applied loading rate, while t^f is dominated by the failure process, which is dependent on the size of the sample and the stress-state prior to the onset of failure. Equating the energy densities from (13) and (14), we obtain:

$$t^f = \left(\frac{2C\Gamma}{M^2 v_c E\dot{\epsilon}^2}\right)^{1/3} \tag{15}$$

Making the appropriate substitutions for t^f into equation (12), the rate-dependent average fragment size is derived as:

$$\hat{L}_{Grady} = 2v_c t^f = 2v_c\left(\frac{2C\Gamma}{M^2 v_c E\dot{\epsilon}^2}\right)^{1/3} = 2\left(\frac{2CK_{Ic}^2 v_c^2}{M^2 E^2\dot{\epsilon}^2}\right)^{1/3} \tag{16}$$

In the normalized size and strain rate form:

$$\bar{\hat{L}}_{Grady} = 2\left(\frac{2Cv_c^2}{M^2 c^2\bar{\dot{\epsilon}}^2}\right)^{1/3} \tag{17}$$

We can also make similar modifications to the Glenn and Chudnovsky [9], to arrive at a *non-normalized* prediction of:

$$\hat{L}_{GC} = 4\sqrt{\frac{3}{\zeta}}\sinh\left(\frac{\phi}{3}\right) \tag{18}$$

where

$$\phi = \sinh^{-1}\left[\beta\left(\frac{3}{\zeta}\right)^{3/2}\right] \tag{19}$$

and

$$\zeta = \frac{2Cv_c^2\sigma_t^2}{M^2c^2\rho E\dot{\epsilon}^2} \tag{20}$$

$$\beta = \frac{2Cv_c^2\Gamma}{M^2c^2\rho\dot{\epsilon}^2} \tag{21}$$

We make these modifications to the Glenn and Chudnovsky [9] model because we believe that the size should become strain-rate independent (plateau) for low strain rates, which the Grady [8] does not account for.

To obtain model predictions, values for the fracture toughness (K_{Ic}) and Young's modulus (E) are used (Table 1), in addition to the crack speed (v_c) and M measurements that are presented in Table 2. We also list the minimum fragment size considered in the structural-controlled regime ($\ell_{II\ min}$). The boron carbide crack speeds have been updated since Hogan et al. [15] as a result improved camera resolution and sample surface finish. Crack speeds for spinel are from Kimberley and Ramesh [17], basalt from Hogan et al. [21], and GRO 85209 from Hogan et al. [35]. Calculated values for the characteristic size and strain rate are also displayed in Table 2 for each material (note they are all different), and these are used in plotting models predicting the rate-dependent average fragment size. We take M=2 and this is motivated by our experimental com-

pressive fragmentation results. Later we take C=2 because we assume an expanding ring problem.

Before presenting the rate-dependent average fragment size we briefly consider the uncertainty in the mechanical properties used to calculate the characteristic length size and strain rate. While σ_t is taken to be 1/10 of the quasi-static compressive strength here, the handbook by Charles [42] indicates that it may vary between 1/8 and 1/12. Thus we assign an uncertainty to σ_t of 20 %. E and ρ are measured experimentally and are typically known to within an uncertainty of 5 %. K_{Ic} is normally provided by the producer of the ceramic materials, and are assumed for basalt and GRO 85209 based on values from the literature. However, substantial variability exists in each case. Based on experience, we assume an uncertainty of 20 % in K_{Ic} for the ceramics and 40 % for the rocks. Considering the possible combinations of uncertainties, minimum and maximum values for the characteristic size and strain rate are listed in brackets in Table 2.

4.2. Experimental Comparison

4.2.1. Compressive Fragmentation Framework

Next, we present a framework for comparing the compressive brittle fragmentation experiments with the tensile fragmentation predictions described in the previous subsection. The comparison of the measured sizes with models requires the definition of an equivalent tensile strain rate ($\dot{\epsilon}_{equi}$), since the models all assume tension. This is achieved here through an energy equivalence argument, wherein the strain energy in compression, W, is converted to the kinetic energy of an expanding ring, KE_{ring}. In this, one can define an equivalent tensile strain rate of the expanding ring as:

$$\dot{\epsilon}_{equi} = \frac{U}{R} \tag{22}$$

where R (m) is the equivalent expanding ring radius and U (m/s) is the velocity expansion of the equivalent expanding ring. U is estimated by assuming that the strain energy in compression is converted to the kinetic energy of an expanding ring. The strain energy (W) in compression is given as:

$$W = \left[\frac{1}{2}\int \sigma d\epsilon\right]\nabla = \frac{1}{2}\frac{\sigma^2 L^3}{E} \tag{23}$$

where ϵ is the strain, σ is the peak compressive stress (Pa) (can be rate-dependent), ∇ is the volume (m^3) and L is a characteristic specimen size (m) (here we are assuming a cube). We note that t^{ℓ} is implicitly considered in σ. The kinetic energy of an equivalent expanding ring is given as:

$$KE_{ring} = \frac{1}{2}mU_{ring}^2 = \frac{1}{2}\rho\pi RT^2 U_{ring}^2 \tag{24}$$

where m is the mass of the specimen of the expanding ring (kg), and T is thickness of the ring (m). We assume that the volumes of the cubes and the expanding ring are the equivalent such that:

$$L^3 = \pi RT^2 \tag{25}$$

Equating W=KE_{ring} and solving for U_{ring}:

$$U_{ring} = \sqrt{\frac{\sigma^2}{\rho E}} \tag{26}$$

and correspondingly our estimate of the equivalent tensile strain rate for our compression experiment is

$$\dot{\epsilon}_{equi} = \frac{U_{ring}}{R} = \sqrt{\frac{\sigma^2}{\rho E R^2}} \tag{27}$$

In accordance with the thin expanding ring assumption, we take $R = 10T$, and assuming volume equivalence (thus maintaining energy densities), we determine $R = L(100/\pi)^{1/3}$. Note that conclusions remain the same with $R = 100T$ (i.e., models adequately describe ceramics, while rocks are slightly over-predicted). Unfortunately, the $R = fn(L)$ assumption introduces a geometric term into the model. We have attempted to define thickness of the ring T in various ways, while still computing R through volume equivalence. Defining $T = v_c t_0$ results in nonphysical small thickness of the ring, while defining $T = v_c t^f$ results in an nonphysical large thickness. Assuming $R \geq 10T$ and computing R using the volume equivalence, the equivalent tensile strain rate can be estimated. We plot our average fragment sizes against this computed equivalent tensile strain rate from equation (27). Since the models do not account specifically for microstructure, we compare only the average fragment size in the Regime II (the structure-dependent regime).

4.2.2. Comparison of Model and Experiments

We now compare the tensile fragmentation models to our experimental compressive fragmentation results using the framework previously described. A summary of the experimental measures is provided in Table 3. These include: the lower limit fragment size from the structure-dependent fragmentation regime ($\ell_{II\ min}$) (determined from scatter plots of circularity vs. size such as Figure 5); the average fragment size ($\hat{\ell}$) in the structure-dependent regime, together with its standard deviation; the measured uniaxial compressive strength (σ), the compressive strain rate at which that experiment was performed ($\dot{\epsilon}_{comp}$), and the equivalent tensile strain rate ($\dot{\epsilon}_{equi}$) estimated from equation (27). We also present the normalized average fragment size ($\bar{\hat{\ell}}$) and strain rate ($\bar{\dot{\epsilon}}_{comp}$).

Figure 6 shows the comparison of the experimental results (using the framework

to compute the strain rate) with the models. The large error bars stem from the uncertainties associated with the mechanical properties. The normalized size predictions by Grady [8], Glenn and Chudnovsky [9], Zhou et al. [10, 11] and Levy and Molinari [12] are also shown, as well as our modified versions of the Grady [8], and Glenn and Chudnovsky [9] models. To compute the model curves, material properties for SiC-N are used. The modified Glenn and Chudnovsky [9] model tracks with the modified Grady [8] model for higher strain rates. Both of the modified models predict smaller fragment sizes than all of the other models for higher strain rates. A comparison of the experiments and models demonstrates the modified Grady [8] model appears to track the best with the experimentally available data, with the average size for the rocks being slightly over-predicted. The modified Glenn and Chudnovsky [9] model and the models by Zhou et al. [10, 11] and Levy and Molinari [12] also fit the data adequately. Additional compression experiments are needed to provide further insight into the fits of the models for the low strain-rate regime.

Lastly, we note that in some past impact fragmentation studies by Hogan et al. [22, 43], it was concluded that the Glenn and Chudnovsky [9], Zhou et al. [10, 11] and Levy and Molinari [12] models were sufficient to predict the impact fragmentation of rock. However, in those studies we did not have a good measure of the fundamental material properties (which are well-characterized in this paper). Furthermore, the corresponding average fragment sizes were plotted at a nominal strain rate estimated as the ratio of impact velocity and target thickness. This is an inaccurate estimate of the time-varying compressive strain rate in such impacts, and this should be converted to an equivalent tensile strain-rate in order to compare with tensile fragmentation models. Similarly, in their experimental study on the uniaxial compression of SiC-N, Wang and Ramesh [44] plot their average fragment size against the compressive loading rates, which is incorrect

when comparing to the tension models. Lastly, in a recent review paper for the planetary science community by Ramesh et al. [27], fragmentation results for basalt were plotted by assuming that R is 10x the specimen length (L). Similar assumptions were made for boron carbide [15]. The current paper assumes a volume equivalence argument, which results in R being approximately 3.2x the specimen length (i.e., $R = L(100/\pi)^{1/3}$).

4.3. Structure-Dependent Fragmentation Size Distributions

Lastly, the distributions of fragment sizes in the structure-dependent regime (Regime II) are investigated. The distributions for the microstructure-controlled (Regime I) are not investigated because of our uncertainty in the size measurements for fragments < 20 μm, although their distributions are believed to be closely related to the defect spacing distributions [28]. The origins of various functional forms for the fragment size distribution are presented in the reviews by Åström [45] and in the book chapter by Grady [29]. Early works qualifying fragment size distributions used statistical and geometric approaches to predict fragmentation distribution shapes [46–48]. For brittle materials, exponential distributions of fragment sizes arise from a Poisson process, where cracks are assumed to not interact. Power-law distributions arise from a cascade of breakups and self-similarity [49]. Much interest in brittle fragmentation has been focused on power-law fragment size distributions because of its links to scale-invariance [50]. Log-normal distributions [44] and two-parameter Weibull functions have also been used to describe fragmentation distributions [51].

Figure 7a shows the cumulative distributions of fragment sizes from our experiments for structure-controlled fragmentation of silicon carbide for quasi-static and dynamic rates. Fitted to the experimental data are power-law distributions curve fits in the form

proposed by Grady [52]:

$$G(\ell_i) = \frac{1}{1 + \left(\frac{\ell_i - \ell_{II\ min}}{a}\right)^b} \tag{28}$$

where $\ell_{II\ min}$ is the minimum fragment size in the structural-controlled regime, and a and b are scaling parameters. As expected, the experimental silicon carbide distributions (blue lines) shift to the left for increasing strain-rate (Figure 7a). As discussed before, this is a result of additional strain energy for higher strain-rate compression and associated increase in the activation of defects. The power-law fit in the form of equation (28), with the coefficients a and b provided in Table 4, describes the silicon carbide fragment size distributions well (black lines). Note that values for $\ell_{II\ min}$ are shown in Table 2. Also shown in Figure 7a using the red solid line is a Rayleigh distribution fit for the quasi-static experiment. This Rayleigh distribution was used by Zhou et al. [10] to describe fragment sizes for expanding brittle ring simulations and has the same form as equation (29) with b=2. The scaling parameter for the Rayleigh distribution fit to this data is a=280 μm. The Rayleigh distribution does not describe our experimental compressive fragmentation results sufficiently. We note that it is reasonable to expect other distributions may describe other loading conditions (e.g., blast), and stress-states (tension).

For our experimental compressive fragmentation results, a power-law-like functional form describes all materials, except for spinel. For spinel, the fragmentation distributions are better described by the exponential distribution:

$$F(\ell_i) = 1 - exp\left(- \frac{\ell_i - \ell_{II\ min}}{a} \right)^b \tag{29}$$

We show the quasi-static cumulative distribution for spinel in Figure 7b. The spinel materials considered by Kimberley and Ramesh [17] were designed to have good trans-

parency and so have the smallest defects and the fewest number of defects of any materials studied here, and this may contribute to the fragment sizes following an exponential distribution (since the interaction of cracks is likely weak). Lastly, we show the cumulative distribution of the meteorite GRO 85209 (purple-to the right) in Figure 7b. For the GRO 85209 material, the experimental sizes are slightly smaller (curve is to the left) than the best fit of the power-law. Similar trends are observed in basalt, and this is likely a result of retarded crack growth due to increased porosity and plasticity in the rock materials (making fragments smaller in a relative sense).

Lastly, the trends for scaling and power-law coefficients in Table 4 are briefly discussed. Values of a and $|b|$ decrease for increasing strain. Both are a result of the smaller fragments representing a greater proportion of the fragment population. With the exception of the silicon carbide example, the decrease in a is greater (higher ratio) for increasing strain rate than for b.

5. Discussion

A framework was presented for comparing the average compressive brittle fragmentation size with well-known modified tensile fragmentation theories. Reasonable agreement was found between theory and experimental results. This is important because the model provides insight into how one can control fragmentation outcomes by tailoring the microstructure and mechanical properties. This may be used in, for example, the design of ceramic materials for ballistic applications, where fragment may be an indicator of ballistic performance [1]. In this study, we have also shown that the fragment size *distributions* may depend on the stress-state (comparison of our distribution and the Zhou et al. [10] tensile fragment size distribution). This is likely a consequence of three factors that distinguish tensile and compressive brittle fragmentation, manifesting

in experimental results:

1. The initial compressive stresses create and grow internal defects in the microstructure, whereas this are not assumed to be as prevalent in tension. Current fragmentation models, including the modified versions presented here, do not account for this.
2. The quantitative micro-mechanics associated with the direction of crack propagation may be different in tension than in compression. In uniaxial compression, wing-cracks [13, 14] grow from a *distribution* of flaws in a stable manner in the direction of maximum compression. Micro-cracking due to wing-cracks is triggered by the deviatoric component of the stress state, and is relatively amplified under uniaxial compression, compared to confined compression. In uniaxial tension, unstable crack growth from a few flaws occurs in directions normal to the maximum tensile stress. Wing-crack growth is believed to be responsible for defect nucleation in Regime II, and the spacing between them appears to influence the fragments sizes in Regime I.
3. A consequence of stable wing-crack growth in compression is that strengths (and subsequently the strain energies) are an order of magnitude larger in compression than in tension. The ability of the brittle material to absorb more strain energy stored in compression than in tension results in more energy being available for fragmentation (resulting in smaller fragments). Currently, this is accounted for using the energy equivalence argument that is presented in this paper. This has implications in the current use of such models since existing approaches commonly use analytical or computational models for the case of uniaxial tension stress state for interpreting experimental results for impact or explosive loading conditions, despite these applications being predominantly a consequence of com-

pressive failure.

Implicit in any analytical and most computational approaches is also the assumption that a purely tensile stress-state exist at a unique homogeneous deformation rate, which is also not often the case. Experiments and real-world loading scenarios involve highly heterogeneous deformation rates and a wide range of stress states, including compressive states that predominate under impact loading, as in the widely considered terminal ballistic problem. There have been limited experimental studies for impact-induced fragmentation, but the complexity of the time evolving stress-state and strain-rate renders it non-trivial to capture these complex failure processes in a predictive model for fragmentation outcomes.

6. Conclusions

In this study, we have investigated the fragmentation of brittle materials under compression, which we recognize plays an important role in the numerous fragmentation applications that undergo very large initial compressive deformations (e.g., impact). We developed a modified energy-based framework for describing compressive fragmentation results with tensile fragmentation theories. Reasonable agreement was found. The development of predictive capabilities for compressive brittle fragmentation outcomes can be useful in applications where compressive stress state dominates. Example include the design of new ceramic and glass materials [1] and in predicting the outcome of impact events that have helped shape our solar system [2].

7. Acknowledgments

Research was sponsored by the Army Research Laboratory and was accomplished under Cooperative Agreement Number W911NF-12-2-0022. The views and conclu-

sions contained in this document are those of the authors and should not be interpreted as representing the official policies, either expressed or implied, of the Army Research Laboratory or the U.S. Government. The U.S. Government is authorized to reproduce and distribute reprints for Government purposes notwithstanding any copyright notation herein. Matt Shaeffer is thanked for helping to facilitate the experiments, as well as providing the high-speed photographs used in this study. Jamie Kimberley, Eswar Prasaad, and Angela Stickle are credited with performing some experiments to generate fragments.

8. References

[1] A. Krell, E. Strassburger, Order of influences on the ballistic resistance of armor ceramics and single crystals, Materials Science and Engineering: A 597 (0) (2014) 422 – 430.

[2] P. Michel, P. Tanga, W. Benz, D. C. Richardson, Formation of asteroid families by catastrophic disruption: Simulations with fragmentation and gravitational reaccumulation, Icarus 160 (1) (2002) 10–23.

[3] J. A. Sanchidrian, P. Segarra, L. M. López, Energy components in rock blasting, International Journal of Rock Mechanics and Mining Sciences 44 (1) (2007) 130–147.

[4] J. D. Hogan, J. G. Spray, R. J. Rogers, G. Vincent, M. Schneider, Dynamic fragmentation of planetary materials: ejecta length quantification and semi-analytical modelling, International Journal of Impact Engineering 62 (2013) 219–228.

[5] J. D. Hogan, R. J. Rogers, J. G. Spray, S. Boonsue, Fracture and fragmentation of

quartz and albite during single-diamond sliding-point contact, Engineering Fracture Mechanics 96 (0) (2012) 165 – 178.

[6] N. Mott, A theory of the fragmentation of shells and bombs, Technical Report AC4035, United Kingdom Ministry of Supply (May 1943).

[7] N. Mott, Fragmentation of shell cases, Technical Report A189: 300308, Proceedings of the Royal Society (1947).

[8] D. E. Grady, Fragmentation of rings and shells: the legacy of N.F. Mott, Springer, 2006.

[9] L. A. Glenn, A. Chudnovsky, Strain and energy effects on dynamic fragmentation, Journal of Applied Physics 59 (4) (1986) 1379 –1380.

[10] F. Zhou, J. F. Molinari, K. T. Ramesh, Analysis of the brittle fragmentation of an expanding ring, Computational Materials Science 37 (1-2) (2006) 74 – 85.

[11] F. Zhou, J. F. Molinari, K. T. Ramesh, Effects of material properties on the fragmentation of brittle materials, International Journal of Fracture 139 (2006) 169–196.

[12] S. Levy, J. Molinari, Dynamic fragmentation of ceramics, signature of defects and scaling of fragment sizes, Journal of the Mechanics and Physics of Solids 58 (1) (2010) 12 – 26.

[13] S. Nemat-Nasser, H. Horii, Compression-induced nonplanar crack extension with application to splitting, exfoliation, and rockburst, Journal of Geophysical Research 87 (B8) (1982) 6805–6821.

[14] L. Farbaniec, J. Hogan, K. Ramesh, Micromechanisms associated with the dynamic compressive failure of hot-pressed boron carbide, Scripta Materialia.

[15] J. D. Hogan, L. Farbaniec, M. Shaeffer, K. Ramesh, The effects of microstructure and confinement on the compressive fragmentation of an advanced ceramic, Journal of the American Ceramic Society 98 (3) (2015) 902–912.

[16] H. Wang, K. T. Ramesh, Dynamic strength and fragmentation of hot-pressed silicon carbide under uniaxial compression, Acta Materialia 52 (2) (2004) 355–367.

[17] J. Kimberley, K. T. Ramesh, Dynamic response of transparent ceramic mgal$_2$o$_4$ spinel, Scripta Materialia 65 (9) (2011) 830–833.

[18] Z. Tang, M. B. Abrams, J. C. Mauro, L. R. Zoeller, N. Venkataraman, G. Hu, High-speed camera study of stage iii crack propagation in chemically strengthened glass, Applied Physics A (2014) 1–7.

[19] B. Lin, M. Mear, K. Ravi-Chandar, Criterion for initiation of cracks under mixed-mode i+ iii loading, International journal of fracture 165 (2) (2010) 175–188.

[20] A. Momber, Fractal dimensions of cement-based composites after mechanical comminution, International Journal of Mineral Processing 110111 (0) (2012) 82 – 89.

[21] J. D. Hogan, J. Plescia, C. El Mir, K. T. Ramesh, Dynamic brittle fragmentation: Probing the byproducts of hypervelocity impact in space, in: 2015 Hypervelocity Impact Symposium (HVIS 2015), Boulder, USA, 2015.

[22] J. D. Hogan, J. A. Castillo, A. Rawle, J. G. Spray, R. J. Rogers, Automated mi-

croscopy and particle size analysis of dynamic fragmentation in natural ceramics, Engineering Fracture Mechanics 98 (0) (2013) 80 – 91.

[23] M. Bakas, V. Greenhut, D. Niesz, J. Adams, J. McCauley, Relationship between defects and dynamic failure in silicon carbide, in: 27th Annual Cocoa Beach Conference on Advanced Ceramics and Composites-A: Ceramic Engineering and Science Proceedings, Vol. 268, Wiley. com, 2009, p. 351.

[24] M. Bakas, J. W. McCauley, V. Greenhut, D. Niesz, R. Haber, B. West, Quantitative analysis of inclusion distributions in hot pressed silicon carbide, International Journal of Impact Engineering 50 (2012) 40–48.

[25] E. V. Ryan, Asteroid fragmentation and evolution of asteroids, Annual Review of Earth and Planetary Sciences 28 (1) (2000) 367–389. doi:10.1146/annurev.earth.28.1.367.

[26] Q. Zhang, J. Zhao, A review of dynamic experimental techniques and mechanical behaviour of rock materials, Rock Mechanics and Rock Engineering (2013) 1–68.

[27] K. Ramesh, J. D. Hogan, J. Kimberley, A. Stickle, A review of mechanisms and models for dynamic failure, strength, and fragmentation, Planetary and Space Science 107 (2015) 10–23.

[28] J. Hogan, J. Plescia, K. T. Ramesh, Failure and fragmentation of meteorites and basalt: Understanding lunar regolith generation, in: Lunar and Planetary Institute Science Conference Abstracts, Vol. 45, 2014, p. 2426.

[29] D. Grady, Dynamic fragmentation of solids, in: Shock Wave Science and Technology Reference Library, Vol. 3, Springer Berlin Heidelberg, 2009, pp. 1–108.

[30] J. Kimberley, K. T. Ramesh, N. P. Daphalapurkar, A scaling law for the dynamic strength of brittle solids, Acta Materialia 61 (9) (2013) 3509–3521.

[31] J. D. Hogan, L. Farbaniec, T. Sano, M. Shaeffer, K. Ramesh, The effects of defects on the uniaxial compressive strength and failure of an advanced ceramic, Acta Materialia 102 (2016) 263–272.

[32] A. Krell, J. Klimke, T. Hutzler, Advanced spinel and sub-μm al 2 o 3 for transparent armour applications, Journal of the European Ceramic Society 29 (2) (2009) 275–281.

[33] A. Stickle, J. Kimberley, K. T. Ramesh, Dynamic strength experiments on basalt with applications to cratering on mercury, in: Lunar and Planetary Institute Science Conference Abstracts, Vol. 44, 2013, p. 3021.

[34] J. N. Grossman, The meteoritical bulletin, no. 76, 1994 january: The u.s. antarctic meteorite collection*, Meteoritics 29 (1) (1994) 100–143.

[35] J. D. Hogan, J. Kimberley, K. Hazeli, J. B. Plescia, K. T. Ramesh, Dynamic behavior of an ordinary chondrite: the effects of microstructure on strength, failure and fragmentation, submitted to Icarus ICARUS-14128.

[36] M. Balme, V. Rocchi, C. Jones, P. Sammonds, P. Meredith, S. Boon, Fracture toughness measurements on igneous rocks using a high-pressure, high-temperature rock fracture mechanics cell, Journal of Volcanology and Geothermal Research 132 (23) (2004) 159 – 172.

[37] A. Tonge, K. T. Ramesh, O. Barnouin, Large impacts on airless bodies: The

himeros event on eros, in: Lunar and Planetary Institute Science Conference Abstracts, Vol. 45, 2014, p. 1998.

[38] Simulink, 2013 Matlab User Manual.

[39] M. Ashby, S. Hallam, The failure of brittle solids containing small cracks under compressive stress states, Acta Metallurgica 34 (3) (1986) 497 – 510.

[40] G. Camacho, M. Ortiz, Computational modelling of impact damage in brittle materials, International Journal of Solids and Structures 33 (20-22) (1996) 2899–2938.

[41] W. Drugan, Dynamic fragmentation of brittle materials: analytical mechanics-based models, Journal of the Mechanics and Physics of Solids 49 (6) (2001) 1181 – 1208.

[42] A. Charles, Handbook of ceramics, glasses, and diamonds (2001).

[43] J. D. Hogan, R. J. Rogers, J. G. Spray, S. Boonsue, Dynamic fragmentation of granite for impact energies of 6 to 28 j, Engineering Fracture Mechanics 79 (0) (2012) 103 – 125.

[44] H. Wang, K. T. Ramesh, Dynamic strength and fragmentation of hot-pressed silicon carbide under uniaxial compression, Acta Materialia 52 (2) (2004) 355 – 367.

[45] J. A. Astrom, Statistical models of brittle fragmentation, Advances in Physics 55 (3-4) (2006) 247–278.

[46] C. Lienau, Random fracture of a brittle solid, Journal of the Franklin Institute 221 (4) (1936) 485 – 494.

[47] N. F. Mott, E. H. Linfoot, A theory of fragmentation, Tech. Rep. vol. AC3348, United Kingdom Ministry of Supply, UK (February 1943).

[48] D. Grady, M. Kipp, Geometric statistics and dynamic fragmentation, Journal of Applied Physics 58 (3) (1985) 1210–1222.

[49] J. A. Astrom, Statistical models of brittle fragmentation, Advances in Physics 55 (3-4) (2006) 247–278. doi:10.1080/00018730600731907.

[50] D. L. Turcotte, Fractals and chaos in geology and geophysics, Cambridge University Press, United Kingdom, 1993.

[51] Y. Cheong, G. Reynolds, A. Salman, M. Hounslow, Modelling fragment size distribution using two-parameter weibull equation, International Journal of Mineral Processing 74 (2004) S227–S237.

[52] D. E. Grady, Fragment size distributions from the dynamic fragmentation of brittle solids, International Journal of Impact Engineering 35 (12) (2008) 1557 – 1562, hypervelocity Impact Proceedings of the 2007 Symposium - HVIS 2007.

List of Figures

List of Tables

Table 1: Summary of brittle material properties: density (ρ: kg/m^3), Young's modulus (E: GPa), and fracture toughness (K_{1c}: MPa $\sqrt{m}$).

Material	ρ (kg/m^3)	E (GPa)	K_{1c} (MPa $\sqrt{m}$)	Refs.
Silicon carbide (PAD SiC-N)	3,200	460	4.0	[16, 24]
Boron carbide (PAD B_4C)	2,490	430	2.5	[15]
Spinel	3,570	275	2.1	[17]
Basalt	2,870	70	1.6	[21, 33, 36]
Meteorite (GRO 85209)	3,350	14	1.2	[28, 35]

Table 2: A summary of experimentally measured crack speeds (v_c: m/s), $M=t^f/t^f$ (ratio of loading time to failure time in dynamic compression experiments), and the characteristic size (L_0) and strain rate ($\dot{\epsilon}_0$) provided in Zhou et al. [10, 11]. The values in brackets represent lower and upper bounds for the characteristic terms assuming various uncertainties for the mechanical properties.

Material	v_c (m/s)	M	L_0 (eq 6) (μm)	$\dot{\epsilon}_0$ (eq 7) (s^{-1})
Silicon carbide (PAD SiC-N)	1,700±400	2.38 ± 0.26	80 [35-180]	1.0×10^5 [3.5×10^4-2.9×10^5]
Boron carbide (PAD B_4C)	3,200 ± 1,100	1.88 ± 0.56	35 [15-78]	2.6×10^5 [8.9×10^4-7.5×10^5]
Spinel	1,200	1.92 ± 0.59	24 [10-54]	3.99×10^5 [1.4×10^5-1.1×10^6]
Basalt	650 ± 100	1.81 ± 0.54	800 [200-2,450]	3.53×10^3 [8.8×10^2-1.8×10^4]
Meteorite (GRO 85209)	140 ±40	1.63 ± 0.40	3,674 [918-12,500]	5.4×10^2 [1.3×10^2-2.7×10^3]

Table 3: Summary of minimum structural-controlled fragment size ($\ell_{II\ min}$), average structural-controlled fragment size ($\hat{\ell}$) with standard deviation, associated uniaxial compressive stress (σ) and strain rate ($\dot{\epsilon}_{comp}$) under which the experiment was performed, estimated equivalent tensile strain rate computed from equation (27) ($\dot{\epsilon}_{equi}$). Normalized average fragment size ($\bar{\hat{\ell}}$) and strain rate ($\bar{\dot{\epsilon}}_{comp}$) are also provided. QS: quasi-static, Dyn: dynamic, UC: uniaxial compression.

Material and Strain-Rate	$\ell_{II\ min}$ (μm)	$\hat{\ell}$ (μm)	σ (GPa)	$\dot{\epsilon}_{comp}$ (s^{-1})	$\dot{\epsilon}_{equi}$ (s^{-1})	$\bar{\hat{\ell}}$	$\bar{\dot{\epsilon}}_{comp}$
QS UC SiC-N	60	260 ± 194	3.87	10^{-4}	$7.76\times10^{+3}$	3.25	0.06
Dyn UC SiC-N	60	178 ± 138	5.97	490	$1.20\times10^{+4}$	2.25	0.09
QS UC BC	100	318 ± 214	3.09	10^{-3}	$7.23\times10^{+3}$	9.09	0.02
Dyn UC BC	100	264 ± 195	4.50	360	$1.06\times10^{+4}$	7.54	0.03
QS UC Spinel	50	230± 132	3.31	10^{-4}	$8.13\times10^{+3}$	9.58	0.02
Dyn UC Spinel	50	150± 76	4.7	800	$1.15\times10^{+4}$	6.25	0.02
QS UC basalt	100	370 ± 341	0.449	10^{-3}	$2.44\times10^{+3}$	0.46	0.53
Dyn UC basalt	100	272 ± 217	0.680	940	$3.69\times10^{+3}$	0.34	0.80
QS UC GRO 85209	120	443 ± 314	0.105	10^{-4}	$1.75\times10^{+3}$	0.12	2.36
Dyn GRO 85209	120	384± 334	0.320	200	$3.80\times10^{+3}$	0.10	5.14

Table 4: Summary of fitted values for fragment size distributions a and b. Values are fitted against a power-law function (equation 28) for all materials except for spinel, which are from an exponential function (equation 29). QS: quasi-static, Dyn: dynamic, UC: uniaxial compression.

Material and Strain-Rate	a (μm)	b
QS UC SiC-N	141	-2.00
Dyn UC SiC-N	120	-1.04
QS UC BC	150	-1.78
Dyn UC BC	100	-1.60
QS UC Spinel (exponential)	196	1.33
Dyn UC Spinel (exponential)	68	0.95
QS UC basalt	150	-1.50
Dyn UC basalt	97	-1.40
QS UC GRO 85209	230	-1.97
Dyn GRO 85209	165	-1.59

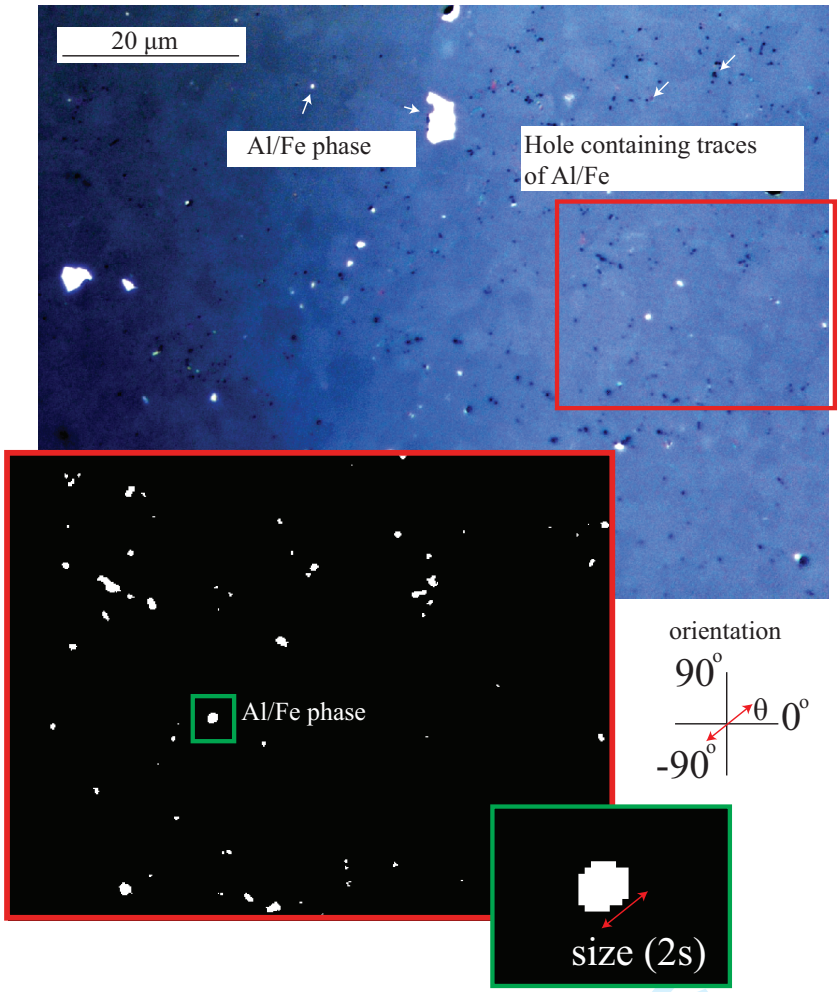

Fig. 1: Optical microscope image of a hot-pressed silicon carbide microstructure with in-set monochrome image of Al/Fe phase (red rectangle) and a further in-set image showing the definition of the defect size, taken as the longest spanning dimension. The defect orientation is also defined, with 0° taken as the horizontal and the orientation angle, θ, as the direction of the longest spanning dimension.

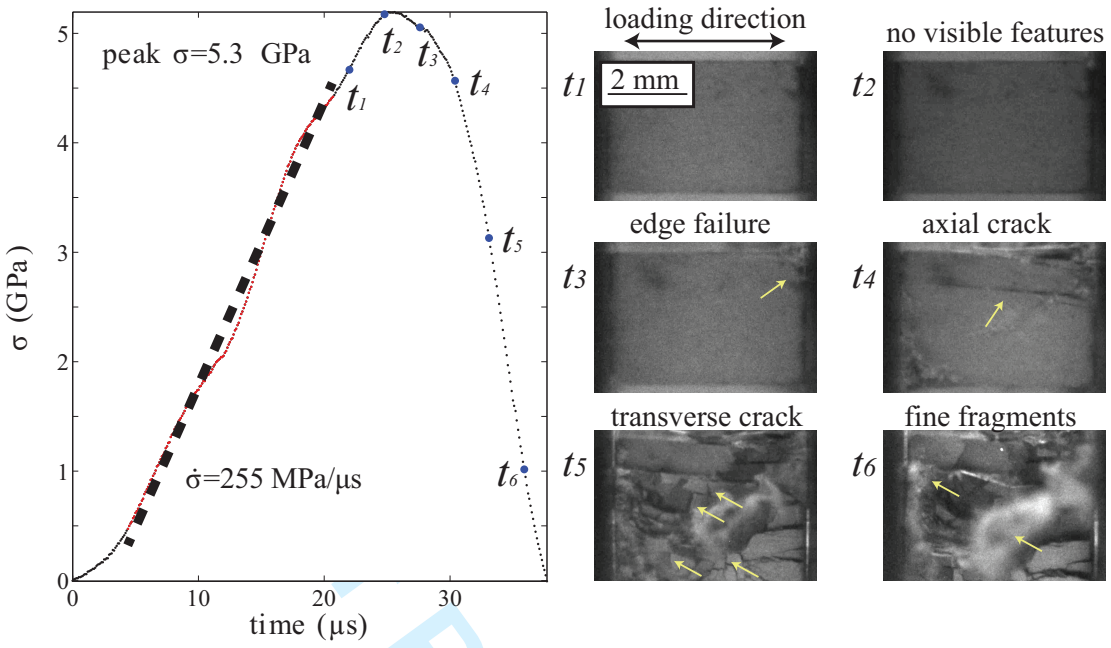

Fig. 2: Stress-time history (left) of dynamic uniaxial compression of silicon carbide with time-resolved high-speed camera images (right) showing mesoscale failure mechanisms. The dashed line on the left is the linear fit of 10 and 90 % of the peak stress, and this corresponds to the stress rate $\dot{\sigma}$=255 MPa/μs.

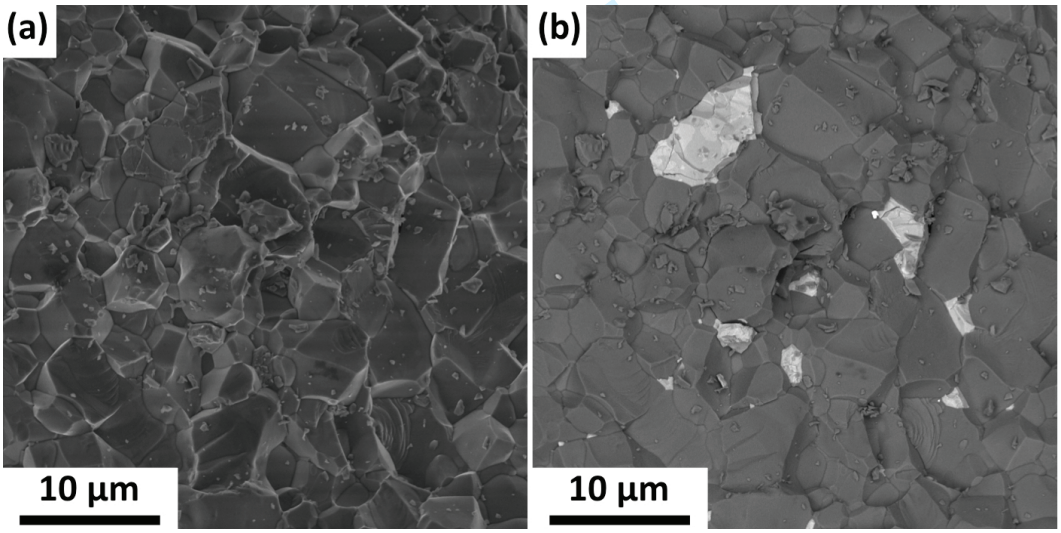

Fig. 3: SEM micrographs showing fracture surface in: (a) secondary electron mode and (b) back-scattered electron mode. A typical intergranular fracture along the grain boundaries was revealed for both: SiC matrix and Al/Fe secondary phases (bright features in figure (b)).

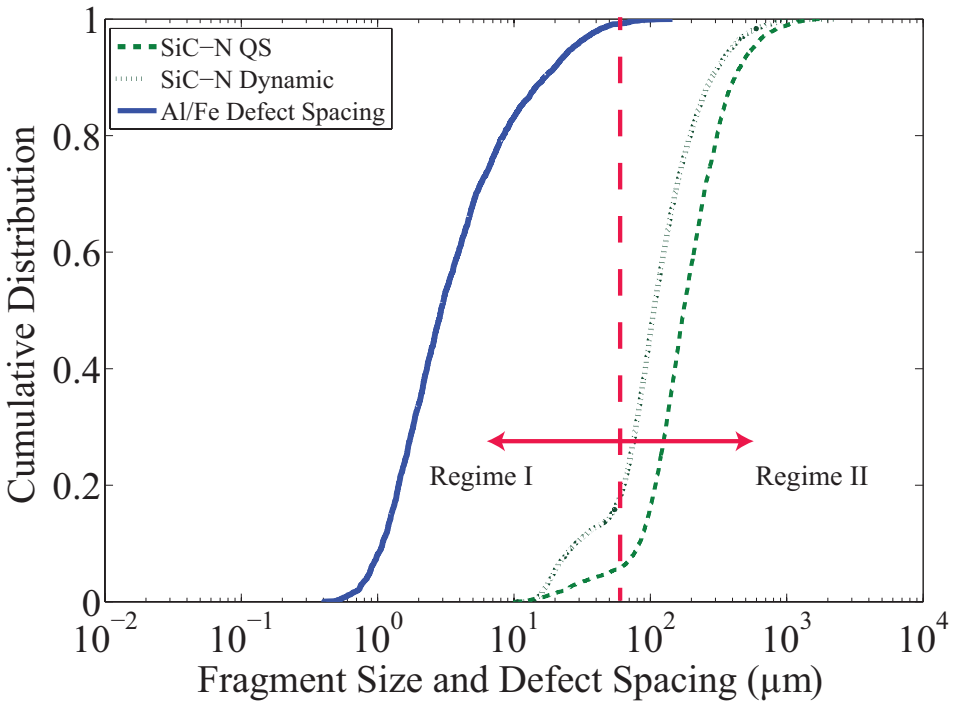

Fig. 4: Cumulative distribution of fragment sizes for strain rates of 10^{-4} (quasi-static) and 490 s^{-1} (dynamic), and spacing between Al/Fe defects. Two fragmentation regimes are labelled where there is an inflection in the size distribution at 60 μm.

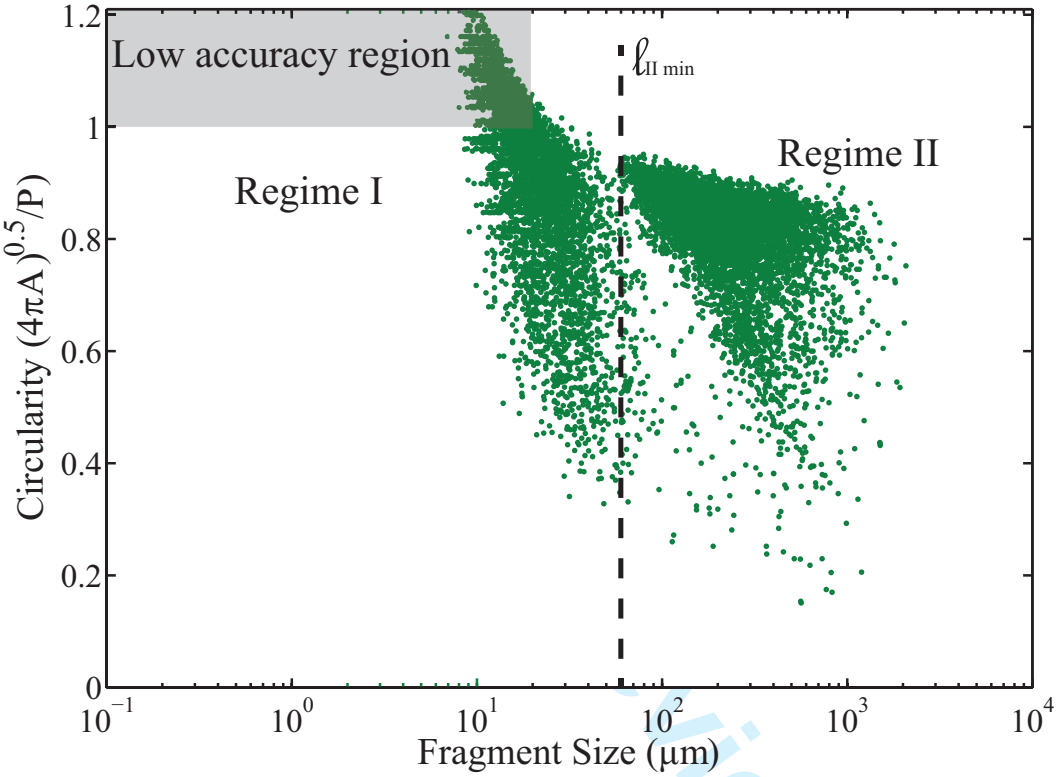

Fig. 5: Scatter plot of circularity vs. fragment size for dynamic uniaxial compression of a hot-pressed silicon carbide. We define the minimum fragment is Regime II as $\ell_{II\ min}$.

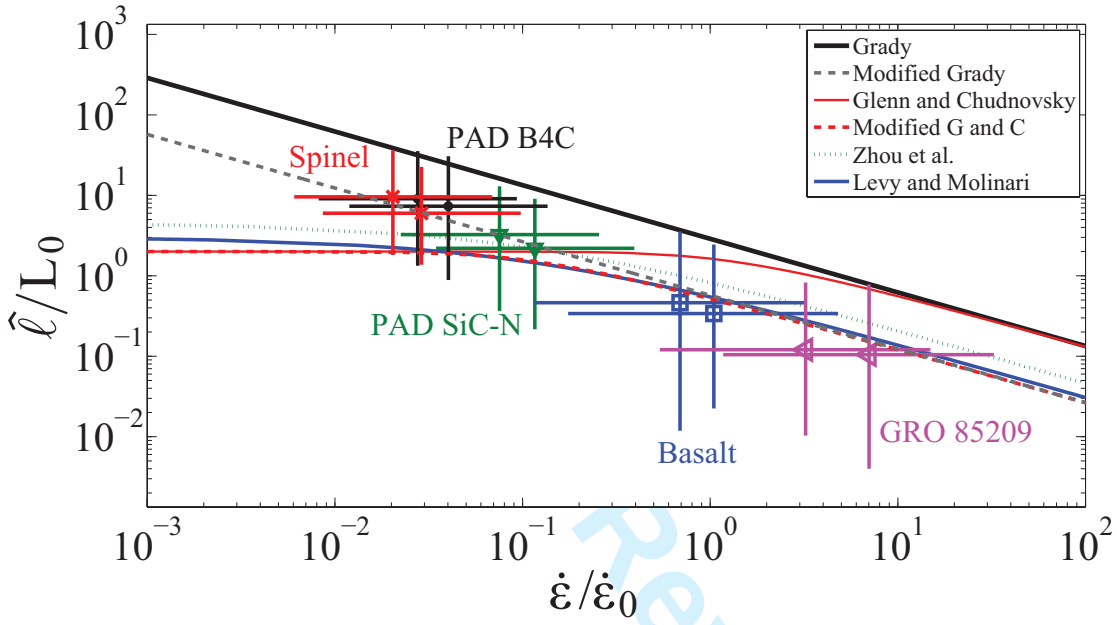

Fig. 6: Comparison of average experimental fragment size of structural-controlled regime with the models of Grady [8], Glenn and Chudnovsky [9], Zhou et al. [10, 11], Levy and Molinari [12], as well as the modified Grady, and Glenn and Chudnovsky models.

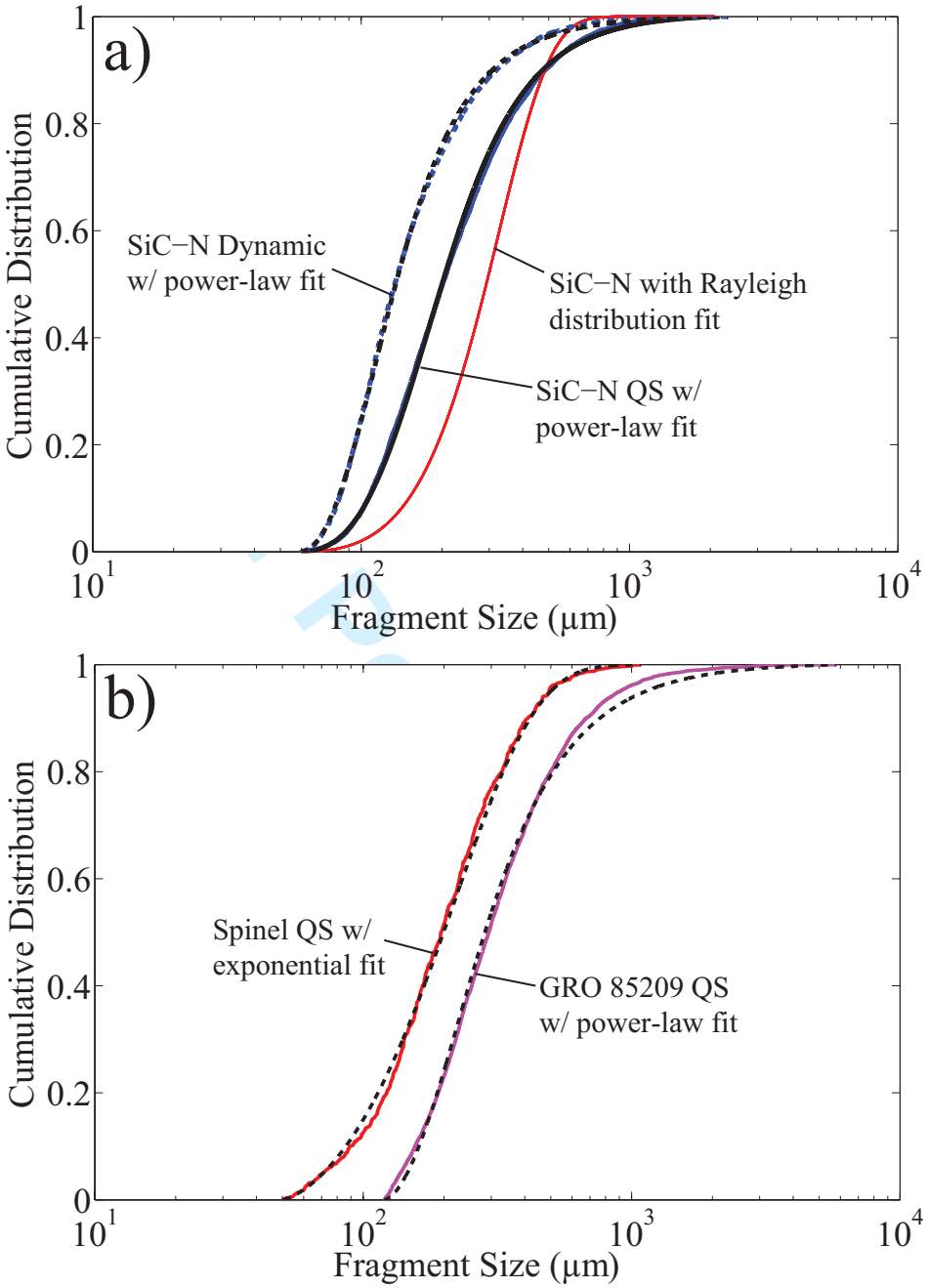

Fig. 7: Experimental cumulative distributions of structural-controlled fragmentation sizes with fits for (a) silicon carbide quasi-static and dynamic experiments (power-law fit- equation 28), and (b) quasi-static experiments for spinel (exponential fit- equation 29) and GRO 85209 (power-law fit- equation 28). Fits for the curves are shown in Table 4.